

Short Communication

Preparation of Low-cost Carbon-supported Mn_3O_4 with a Nano-mesoporous Structure and Its Application in Oxygen Reduction Reactions

Yanjun Wu^{1,2}, Peilan Ma^{2,3}, Ke Shi², Ruinan He², Hong Tang³, Jianping Zeng²,
Yunshan Bai², Wei Wang^{1,2,*}, Song Chen^{2,*}

¹ School of Petrochemical Engineering, Changzhou University, Jiangsu 224051, P.R. China

² School of Chemistry & Chemical Engineering, Yancheng Institute of Technology, Yancheng, Jiangsu 224051, P.R. China

³ Jiangsu Ancan Technology Co. Ltd., Jiangyin, Jiangsu 224051, P.R. China

*E-mail: wangw@ycit.edu.cn; jsyccs@163.com

Received: 18 January 2019 / Accepted: 21 March 2019 / Published: 10 April 2019

Oxygen reduction reactions are of significance because they are the main cathodic reaction in metal-air batteries and fuel cells. In this study, we successfully synthesize a Mn_3O_4/C catalyst with an uncomplicated method. The pore size, distribution, morphology and structure of the Mn_3O_4/C catalyst are studied with scanning electron microscopy, transmission electron microscopy, X-ray diffraction, X-ray photoelectron spectroscopy, and the Brunauer-Emmett-Teller equation. The catalyst activity is investigated by cyclic voltammetry on the gas diffusion electrodes. The result shows the Mn_3O_4/C catalyst has a nano-mesoporous structure and excellent catalytic ability for oxygen reduction reactions.

Keywords: Mn_3O_4/C ; Gas diffusion electrode; Oxygen reduction reaction;

1. INTRODUCTION

With the development of civilization, human demand for energy becomes increasingly intense [1-3]. Fossil fuels have been used as the main energy resource by human beings for centuries. However, after hundreds of years of consumption, fossil energy is on the verge of exhaustion [4,5]. Meanwhile, environmental problems caused by the burning of fossil fuels have threatened the survival of human beings. It is extremely pertinent to seek clean and sustainable energy resources [6]. Hydrogen-oxygen fuel cells are devices that convert chemical energy into electrical energy quickly and efficiently. Usually, hydrogen is used as the anodic reactant and oxygen in air is used as a cathode reactant. The sole product of hydrogen-oxygen fuel cells is water, which has no impact on the environment. Hydrogen-oxygen fuel cells will not give rise to noise pollution for the lack of mechanical transmission devices [7-10]. These

kinds of batteries have high energy density, environmental friendliness and a fast startup rate, so they have very wide application.

For high cathodic overpotential and sluggish oxygen reduction reaction (ORR) kinetics, the reaction process should be catalyzed by catalyst [11, 12]. Precious metals such as platinum, palladium, gold and their alloys have become the best catalysts for oxygen reduction reactions (ORR) for their superior catalytic performance and stability [13]. However, the shortage and high cost of precious metals have limited their industrial application [14]. For this reason, research on nonnoble metal catalysts has become a hotspot. Manganese oxides possess a broad research prospect due to their high catalytic performance for oxygen reduction reactions, abundant reserves and low price [15,16]. They have attracted extensive attention in the energy storage, catalysis, magnetization and adsorption fields. Manganese oxides are expected to replace noble metal materials as the catalysts for ORRs in alkaline media [17]. The synthesis methods for manganese oxides include template synthesis, electrodeposition, hydrothermal synthesis and the sol-gel method [18-20]. Tian Wang et al. [21] synthesized porous graphene@Mn₃O₄ with MgO applied as the template. The prepared materials exhibited comparable catalytic performance to commercial Pt/C catalysts. Pooya Hosseini-Benhangi et al. [22] synthesized active nanostructured MnO_x catalysts for both ORR and OER by anodic deposition. The morphology and crystal structure of MnO_x catalysts were affected by the concentration of Mn²⁺ and the reaction temperature. A anodic potential also impacts the Mn valence, crystal structure, morphology and pore density. The catalytic activity of manganese oxides is closely related to their crystal structure, oxidation state, surface area and active sites [23, 24]. Xiao et al. [25] synthesized Mn₃O₄ for electrochemical capacitors by a hydrothermal approach using hydrazine hydrate as the reducing agent. Activated carbon was added to improve the surface area of the composites, which is conducive to forming an electric double layer. Mn₃O₄/AC composites exhibit excellent performance as materials for electrochemical capacitors. Zhang et al. [26] synthesized Mn₃O₄/C using Vulcan carbon XC-72 as the carbon resources, showing good stability and catalytic performance in oxygen reduction reactions.

It is necessary to do further research on manganese oxides that is promising for replacing precious metal catalysts. In this study, we prepared a Mn₃O₄/C catalyst through a facile redox method using activated carbon as the reducing agent. Activated carbon can be created from almost all carbon-rich organic materials, such as coal, wood, husks, coconut shells and so on. These carbonaceous materials are converted into activated carbon by pyrolysis, gradually forming a complex pore structure. Therefore, low cost, stable chemical properties, large pore volume and surface area, make it a good choice of carbon resources for Mn₃O₄/C composites. Characterization shows that Mn₃O₄/C has large surface area and pore volume. Then, gas diffusion electrodes were prepared with Mn₃O₄/C as the catalyst. Electrochemical measurements were performed on the gas diffusion electrodes and the shows that Mn₃O₄/C catalyst has excellent performance for oxygen reduction reactions (ORR).

2. EXPERIMENTAL SECTION

2.1 Mn₃O₄/C Electrocatalyst preparation

Mn₃O₄/C catalyst was prepared by chemical reduction. 3.16 g of KMnO₄ was dissolved in 200

mL of DI water and the pH was adjusted to 6.0. Then, the solution was heated to 85 °C and 0.60 g of activated carbon was added with thorough stirring. The mixture was stirred for 1 h under 85 °C in a thermostat water bath. The solution was then filtered, washed with 200 mL of DI water, and dried at 100 °C for 12 h. The solid powder was subsequently calcined under 350 °C (heating rate of 5 °C min⁻¹) for 3 h and then the sample was cooled to room temperature.

2.2 Gas diffusion electrode preparation

Preparation of the catalytic layer: 0.5 g of Mn₃O₄/C catalyst, 1.5 g of Vulcan carbon XC-72R, 0.5 g of activated carbon and 0.833 g of PTFE emulsion (60%) were added to 100 mL of absolute ethanol and then stirred until evenly homogenized. Subsequently, the mixture was heated in an 85 °C constant temperature water bath until a mass formed. Then, the agglomerates were rolled into a 0.3 mm thick catalytic layer.

Preparation of the diffusion layer: 2.0 g of acetylene black, 0.5 g of anhydrous sodium sulphate and 2.5 g of PTFE emulsion (60%) were added to 100 mL of absolute ethanol and then stirred until evenly homogenized. Then, the mixture was heated in an 85 °C constant temperature water bath until a mass formed. The agglomerates were then rolled into a 0.3 mm thick diffusion layer.

Preparation of the electrodes: The catalytic layer, nickel mesh and diffusion layer were put together in order, and then cold-pressed for 1 minute at 15 MPa. The electrodes were put into boiling water to remove the anhydrous sulphate, and subsequently, put into a muffle furnace and treated at 250 °C for 1 hour. By calculation, the catalyst loading on the Mn₃O₄/C gas diffusion electrode is approximately 3.0 mg cm⁻². A Pt/C gas diffusion electrode with catalyst loading of 0.3 mg cm⁻² was prepared with the same method.

2.3 Characterization

X-ray diffraction (XRD) measurements were carried out with a PANalytical X'Pert Powder X-ray diffractometer and Cu K α ($\lambda=0.15406$ nm) was used as the radiation source. The scan rate was 5° min⁻¹ and the range was 0°~80°. The tube voltage and current were maintained at 40 KV and 30 mA, respectively. Transmission electron microscopy (TEM) images were performed on a 120 KV JEM-2100F transmission electron microscope to observe the morphology, size and crystal structure of the Mn₃O₄/C. The samples were qualitatively and semi-quantitatively tested using an ESCALAB 250Xi photoelectron spectrometer with monochromatic Al K α radiation. The pore properties and specific surface area of Mn₃O₄/C were tested with a Coulter SA 3100 surface area and pore size analyzer. The samples were outgassed at 120°C and N₂ adsorption isotherms were obtained at liquid nitrogen temperature. The specific surface area was obtained using the Brunauer-Emmett-Teller (BET) equation and the pore structure was analyzed by the Barrett-Joyner-Halenda (BJH) model. The pore surface area was obtained using a t-plot method.

2.4. Electrochemical Characterization

Electrochemical measurements were measured on a CHI660B electrochemical workstation at 1.0 M NaOH electrolyte. A typical three-electrode system was used with gas diffusion electrodes as the working electrode ($S=0.5\text{ cm}^2$), and a saturated calomel electrode (SCE) and platinum slice were used as the reference and the counter electrodes, respectively. Pure O_2 or N_2 was injected into the electrolyte before electrochemical tests to O_2 -saturate the solution or remove dissolved oxygen. The activity of the catalysts was measured using cyclic voltammetry from 0 to -1.0 V at a scan rate of 50 mV s^{-1} . To further research gas diffusion electrode kinetic, cyclic voltammetry was performed at different temperatures, scan rates and O_2 concentrations, respectively.

3. RESULTS AND DISCUSSION

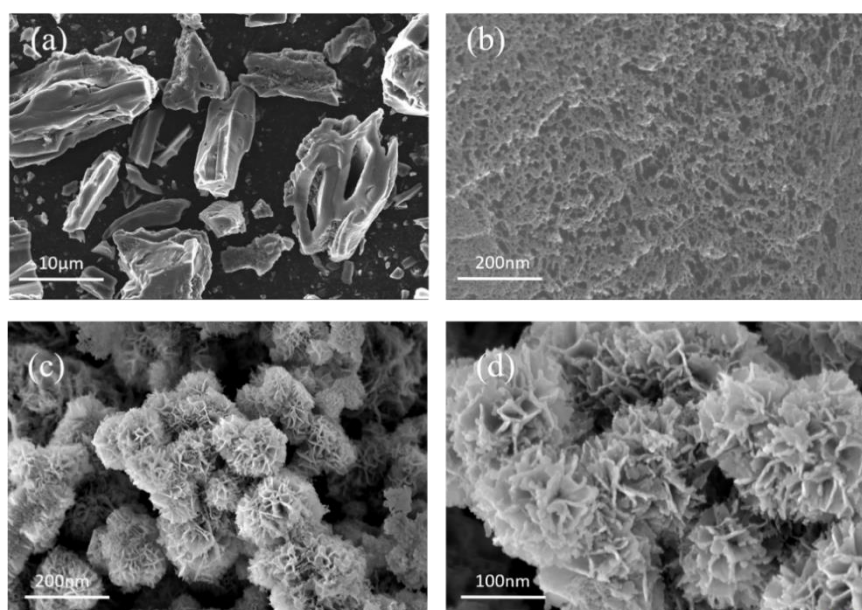


Figure 1. Scanning electron microscopy (SEM) image of (a), (b) activated carbon and (c), (d) $\text{Mn}_3\text{O}_4/\text{C}$.

SEM was performed to observe the activated carbon surface morphology and $\text{Mn}_3\text{O}_4/\text{C}$ catalyst. Figure 1a and 1b show that the activated carbon has an irregular shape with dense pores on the surface, that may provide channels for transmission of electron and material. Figure 1c and d clearly show the ultrathin Mn_3O_4 film with approximately 5 nm average thickness their length is approximately 30-40 nm. The Mn_3O_4 nanoflakes uniformly grow on the activated carbon surface, forming flower-like nanostructures. The flower-like Mn_3O_4 crystals accumulate together, forming high porosity and large surface area. The nanoflake stacking resulted in an overall three-dimensional nanostructure. The high porosity and large surface area provide adequate space for the electrolyte to contact the catalyst, which is a benefit for the oxygen reduction reactions (ORR).

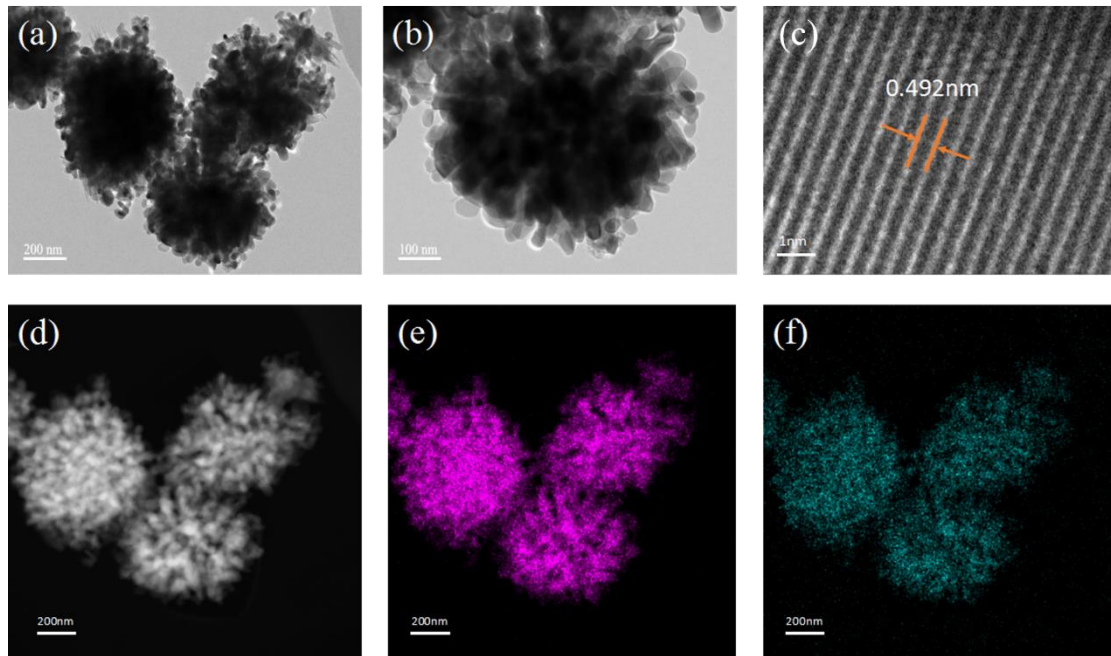


Figure 2. Transmission electron microscopy (TEM) image and EDS elemental maps of Mn_3O_4 . (a), (b) Low magnification TEM image. (c) High magnification TEM image. (d) TEM-EDS mapping of Mn_3O_4 . (e) Mn. (f) O.

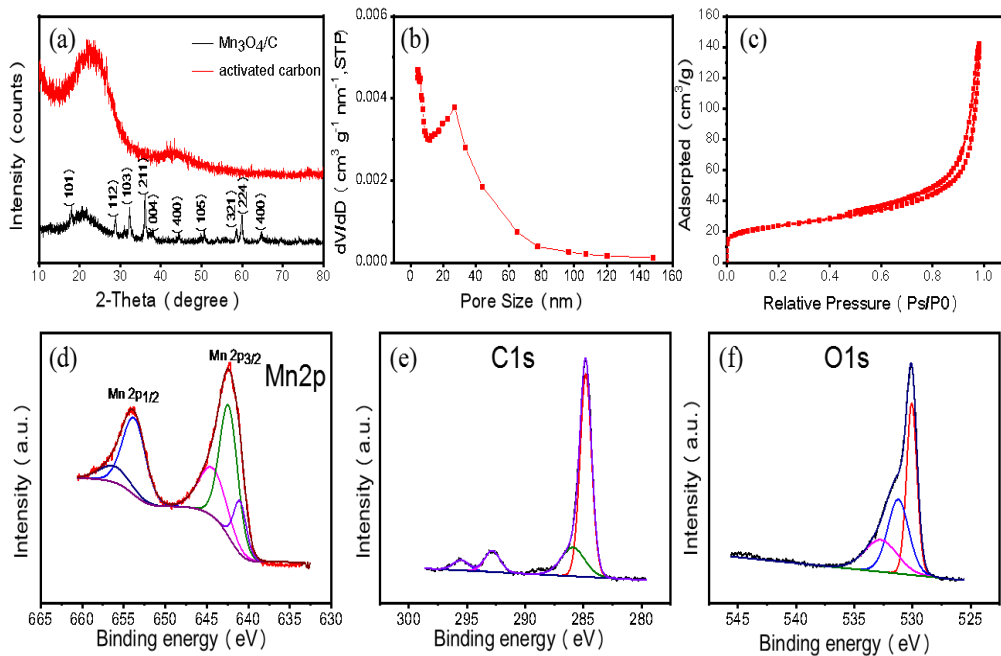


Figure 3. (a) X-ray diffraction (XRD) patterns of activated carbon and $\text{Mn}_3\text{O}_4/\text{C}$. (b) Pore size distribution and (c) nitrogen adsorption isotherms of $\text{Mn}_3\text{O}_4/\text{C}$. (d) Mn 2p XPS spectra, (e) C 1s XPS spectra and (f) O 1s XPS spectra for $\text{Mn}_3\text{O}_4/\text{C}$.

The TEM images of Mn_3O_4 are shown in Figure 2a and 2b. The ultrasonication before the TEM test broke the Mn_3O_4 off of the activated carbon. Because it doesn't adhere to the Formvar/Carbon film due to large particle size the activated carbon cannot be seen in TEM images. The Mn_3O_4 film can clearly

be seen from the TEM images accumulated together to form a three-dimensional nanostructure, corresponding to the SEM result [27]. The size of the three-dimensional nanostructure is approximately 700-800 nm. The distance between two lattice fringes is 0.492 nm, corresponding to the (101) plane of Mn_3O_4 . The mapping images show that the sample contains Mn and O distributed uniformly in the composite.

Figure 3a shows the XRD pattern of activated carbon and $\text{Mn}_3\text{O}_4/\text{C}$. The XRD pattern of activated carbon contains a broad peak at approximately 24° , indicating an amorphous structure and a low graphitization degree. The characteristic diffraction peak of spinel-type (I41/amd) Mn_3O_4 can be seen from the XRD pattern of the sample. Peaks at 18.02° , 28.94° , 32.36° , 36.08° , 38.08° , 44.48° , 50.62° , 58.72° , 59.98° and 64.70° correspond to the (101), (112), (103), (211), (004), (400), (105), (321), (224) and (400) facets and the locations of diffraction peaks are consistent with the standard pattern of Mn_3O_4 (JCPDS card NO.24-0734) [28-30]. The broad peak at approximately 24° can also be seen in the XRD pattern of $\text{Mn}_3\text{O}_4/\text{C}$ and the intensity of the peak is much lower than activated carbon. It may be attributed to the growth of high crystalline Mn_3O_4 on the surface of activated carbon, consistent with the SEM result.

The N_2 adsorption isotherm and BJH desorption pore size distribution of $\text{Mn}_3\text{O}_4/\text{C}$ are shown in Figure 3b and c, respectively. The sample has a type-IV adsorption isotherm followed by an H4 hysteresis loop, indicating that the $\text{Mn}_3\text{O}_4/\text{C}$ contains mesoporous structure [31]. The hysteresis loop closes at a relative pressure of 0.4, indicating that the sample has relatively small mesopores. The existence of a mesoporous structure is attributed to the stacking of three-dimensional nanoflakes. The Brunauer-Emmett-Teller (BET) equation was used to further analyze sample surface area and pore distribution. The result shows that the sample surface area is approximately $84.4 \text{ m}^2 \text{ g}^{-1}$ and the total pore volume is $0.215 \text{ cm}^3 \text{ g}^{-1}$ and the average pore size is 28.9 nm. The large surface area and pore volume provide a large number of active sites and ensure full contact between the materials and electrolyte, which is conducive to the material and electron transmission in oxygen reduction reactions.

Figure 3 shows the $\text{Mn}2\text{p}$, $\text{C}1\text{s}$ and $\text{O}1\text{s}$ XPS spectra for $\text{Mn}_3\text{O}_4/\text{C}$. The $\text{Mn}2\text{p}_{1/2}$ and $\text{Mn}2\text{p}_{3/2}$ peaks can be seen from the $\text{Mn}2\text{p}$ spectra with 11.6 eV binding energy gap. The value of the binding energy gap is consistent with the literature, confirming that the sample mainly contains Mn_3O_4 [32]. The $\text{Mn}2\text{p}$ XPS spectra contains three peaks located at 641.2eV, 642.6eV, and 644.6eV, respectively, corresponding to Mn(II), Mn(III), and Mn(IV) [21]. The high-resolution XPS spectra of the $\text{C}1\text{s}$ region is illustrated in Figure 3e. The $\text{C}1\text{s}$ spectra for $\text{Mn}_3\text{O}_4/\text{C}$ contains two peaks that represent two individual component groups. The peak at 284.7 eV and 285.4eV corresponds to $\text{C}=\text{C}$ and $\text{C}-\text{C}$, respectively. Figure 3f shows the $\text{O}1\text{s}$ XPS spectra for $\text{Mn}_3\text{O}_4/\text{C}$. The forms of O functional groups in $\text{Mn}_3\text{O}_4/\text{C}$ include Mn-O (530.1eV), $\text{C}=\text{O}$ (531.3eV) and $\text{C}-\text{O}$ (532.8eV).

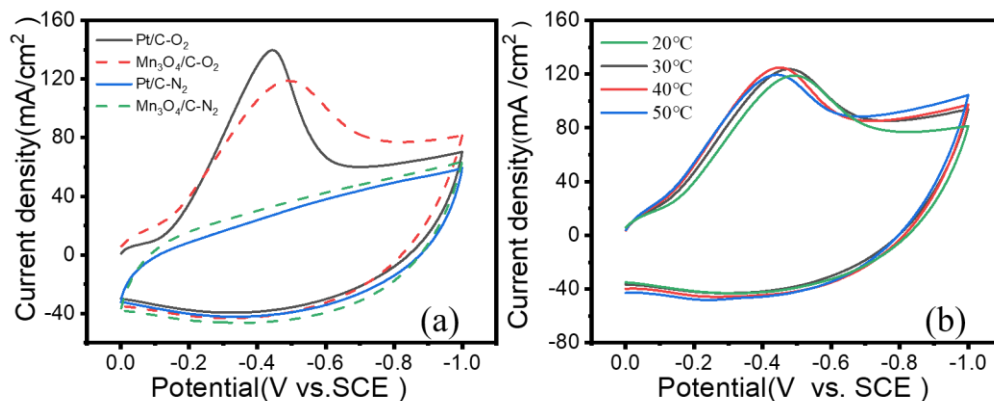


Figure 4. (a) Cyclic voltammograms of Mn₃O₄/C gas diffusion electrode and Pt/C gas diffusion electrode in O₂-saturated or N₂-saturated solutions (b) Cyclic voltammograms of Mn₃O₄/C at 20, 30, 40 and 50 °C, respectively.

Figure 4a shows the ORR activity of Mn₃O₄/C and Pt/C gas diffusion electrodes in O₂-saturated or N₂-saturated 1.0 M NaOH solution at 50 mV s⁻¹ scan rate and room temperature. The CV curves of Pt/C-N₂ and Mn₃O₄/C-N₂ do not show any obvious redox peaks and the background current can be attributed to the charging of the electric double layer [33]. Mn₃O₄/C has higher background current than Pt/C for the specific area of Mn₃O₄/C (84.4 m² g⁻¹) is higher than Pt/C (38 m² g⁻¹) [34]. Single redox peaks appear on the CV curves of Mn₃O₄/C-O₂ and Pt/C-O₂. The onset potential of Mn₃O₄/C is approximately 0.045 V, more positive than Mn₃O₄ (-0.05 V) reported by Zhang et.al [35] and even a little more positive than Pt/C. It can be seen from the CV curves that Pt/C catalyst achieves the maximum of diffusion current density faster than Mn₃O₄/C catalyst and the peak potential of Mn₃O₄/C is slightly more negative than Pt/C. The current density of Mn₃O₄/C approaches 120 mA cm⁻², higher than Mn₃O₄ (74 mA cm⁻²) [35] and only 20 mA cm⁻² lower than Pt/C. It may be attributed to the large pore volume and surface area of the Mn₃O₄/C catalyst, providing large amounts of active sites for oxygen reduction reactions. As seen from the above, the Mn₃O₄/C catalyst has high performance for oxygen reduction reactions. The catalytic performance of Mn₃O₄/C is slightly weaker than Pt/C and its loading is higher than Pt/C. However, the cost of Mn₃O₄/C is much lower, giving it possess research significance and application prospects.

Figure 4b presents the CV curves of the Mn₃O₄/C gas diffusion electrode in O₂-saturated 1.0 M NaOH solution at 50 mV s⁻¹ scan rate and 20, 30, 40 °C, and 50 °C, respectively. When the reaction temperature increases from 20 °C to 30 °C and then to 40 °C, the peak current increases and the peak potential shifts positively, indicating that Mn₃O₄/C has better catalytic activity when the temperature increases. It can be attributed to the rise of oxygen diffusion as the temperature increases, which is similar to the results of Parthasarathy et.al [36]. However, when we continued to raise the reaction temperature to 50 °C, the potential was unchanged but the peak current decreased. The lower oxygen concentration with rising temperature slows down the rate of oxygen reduction reaction. The research of Srinivasan et.al [37] found that the oxygen reduction activity of the gas diffusion electrode does not change significantly when the temperature exceeds 60 °C, which is almost consistent with our results. We

conclude that $\text{Mn}_3\text{O}_4/\text{C}$ has the best catalytic activity at approximately 40 °C.

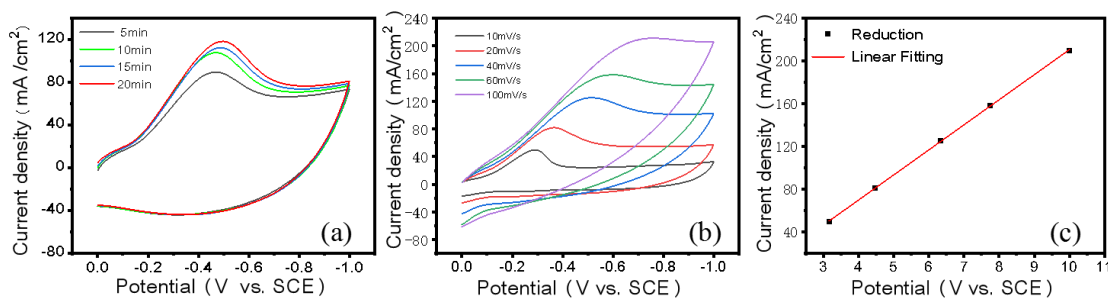


Figure 5. (a) CV curves under different oxygen concentrations (b) CV curves at different scan rates. (C) Relation between scan rate and the reduction peak current on the $\text{Mn}_3\text{O}_4/\text{C}$ gas diffusion electrode.

It can be seen from Figure 5a that oxygen reduction ability is closely related to oxygen concentration. The time of inletting oxygen is set to 5, 10, 15 and 20 min, respectively and the corresponding oxygen concentrations are 6, 7, 8 and 9 mg/L. The oxygen concentration rose and the peak current of the oxygen reduction reaction increased. The process of adsorption and diffusion on the electrode become easier with the oxygen concentration rose, increasing the rate of the oxygen reduction reactions [37]. The oxygen concentration attained saturation after 20 min of feeding oxygen and the current density reached $118.20 \text{ mA cm}^{-2}$.

To further research the oxygen reduction kinetics on the electrode, the CV curves of $\text{Mn}_3\text{O}_4/\text{C}$ in O_2 -saturated 1 M NaOH solution at different scan rates were determined and the results are shown in Figure 5b. It can be seen from the figure that as the scan rate increases, the peak potential of the oxygen reduction reaction shifts significantly, indicating that the oxygen reduction reaction occurring on the electrode is irreversible. Figure 5c shows that the peak current has a good linear relationship with $v^{1/2}$ (v represents the scan rate). The goodness of fit for the linear equation is 0.9998, indicating that the oxygen reduction reaction is controlled by diffusion process [38].

4. CONCLUSIONS

In this study, we successfully synthesized a $\text{Mn}_3\text{O}_4/\text{C}$ catalyst by simple chemical reduction reactions. The physicochemical characterization shows that $\text{Mn}_3\text{O}_4/\text{C}$ has a mesoporous structure with large pore area and volume. The electrochemical tests on the gas electrodes show that $\text{Mn}_3\text{O}_4/\text{C}$ has high catalytic activity for oxygen reduction reactions. The optimal reaction temperature of $\text{Mn}_3\text{O}_4/\text{C}$ catalyst is approximately 40 °C, and the oxygen reduction reaction on the electrode is controlled by diffusion.

ACKNOWLEDGEMENTS

The authors are grateful to the Natural Science Foundation of Jiangsu Province (No. BK20141261).

References

1. T.N. Lambert, J.A. Vigil, S.E. White, C.J. Delker, D.J. Davis, M. Kelly, M.T. Brumbach and M.A.

- Rodriguez, *J. Phys. Chem. C*, 121 (2017) 2789-2797.
2. S. He, D. Ji, P. Novello, X. Li and J. Liu, *J. Phys. Chem. C*, 122 (2018) 21366-21374.
 3. K.R. Yoon, G.Y. Lee, J.W. Jung, N.H. Kim, S.O. Kim and I.D. Kim, *Nano Lett.*, 16 (2016) 2076-83.
 4. J.A. Vigil, T.N. Lambert and K. Eldred, *ACS Appl. Mater. Inter.*, 7 (2015) 22745-50.
 5. G. Li, K. Zhang, B. Han, M.A. Mezaal and L. Lei, *Int. J. Electrochem. Sci.*, 10 (2015) 10554-10564.
 6. S. Deng, T. Meng, B. Xu, F. Gao, Y. Ding, L. Yu and Y. Fan, *ACS Catal.*, 6 (2016) 5807-5815.
 7. G. Yan, Y. Lian, Y. Gu, C. Yang, H. Sun, Q. Mu, Q. Li, W. Zhu, X. Zheng, M. Chen, J. Zhu, Z. Deng and Y. Peng, *ACS Catal.*, 8 (2018) 10137-10147.
 8. S. Thiagarajan, T.H. Tsai, S.M. Chen, *Int. J. Electrochem. Sci.*, 6 (2011) 2235-2245.
 9. G. Qiu, H. Huang, S. Dharmarathna, E. Benbow, L. Stafford and S.L. Suib, *Chem. Mater.*, 23 (2011) 3892-3901.
 10. C.H. Kuo, I.M. Mosa, A.S. Poyraz, S. Biswas, A.M. El-Sawy, W. Song, Z. Luo, S.Y. Chen, J.F. Rusling, J. He and S.L. Suib, *ACS Catal.*, 5 (2015) 1693-1699.
 11. Y.X. Chen and X.B. Ji, *Int. J. Electrochem. Sci.*, 13 (2018) 12155-12162.
 12. H. Xu, Z. Qu, C. Zong, W. Huang, F. Quan and N. Yan, *Environ. Sci. Technol.*, 49 (2015) 6823-30.
 13. S. Yang, Z. Wang, Z. Cao, X. Mao, M. Shi, Y. Li, R. Zhang and Y. Yin, *J. Alloys Compd.*, 721 (2017) 482-491.
 14. M. Zhang, Y.M. Jia and H.W. Li, *Int. J. Electrochem. Sci.*, 13 (2018) 9749-9758.
 15. Y. Meng, W. Song, H. Huang, Z. Ren, S.Y. Chen and S.L. Suib, *J. Am. Chem. Soc.*, 136 (2014) 11452-64.
 16. R. Gao, D. Zhang, P. Maitarad, L. Shi, T. Rungrotmongkol, H. Li, J. Zhang and W. Cao, *J. Phys. Chem. C*, 117 (2013) 10502-10511.
 17. A. Ramirez, P. Hillebrand, D. Stellmach, M.M. May, P. Bogdanoff and S. Fiechter, *J. Phys. Chem. C*, 118 (2014) 14073-14081.
 18. A. Iyer, J. Del-Pilar, C.K. King'ondou, E. Kissel, H.F. Garces, H. Huang, A.M. El-Sawy, P.K. Dutta and S.L. Suib, *J. Phys. Chem. C*, 116 (2012) 6474-6483.
 19. J.H. Kim, K.H. Lee, L.J. Overzet and G.S. Lee, *Nano Lett.*, 11 (2011) 2611-7.
 20. J.S. Lee, G.S. Park, H.I. Lee, S.T. Kim, R. Cao, M. Liu and J. Cho, *Nano Lett.*, 11 (2011) 5362-6.
 21. T. Wang, Q. Le, X. Guo, M. Huang, X. Liu, F. Dong, J. Zhang and Y.X. Zhang, *ACS Sustain. Chem. Eng.*, 7 (2019) 831-837.
 22. P. Hosseini-Benhangi, C.H. Kung, A. Alfantazi and E.L. Gyenge, *ACS Appl. Mater. Inter.*, 9 (2017) 26771-26785.
 23. J. Xu, Y. Sun, M. Lu, L. Wang, J. Zhang, J. Qian and E.J. Kim, *J. Alloys Compd.*, 717 (2017) 108-115.
 24. K. Selvakumar, S.M. Senthil Kumar, R. Thangamuthu, K. Ganesan, P. Murugan, P. Rajput, S.N. Jha and D. Bhattacharyya, *J. Phys. Chem. C*, 119 (2015) 6604-6618.
 25. X. Xiao, Y. Wang, G. Chen, L. Wang and Y. Wang, *J. Alloys Compd.*, 703 (2017) 163-173.
 26. Z. Zhang, D. Zhou, X. Bao, G. Huang, Q. Tang and B. Huang, *J. Alloys Compd.*, 777 (2019) 872-876.
 27. Z. Wang, Q. Qin, W. Xu, J. Yan and Y. Wu, *ACS Appl. Mater. Inter.*, 8 (2016) 18078-88.
 28. G. Deepaa and C.K. Mahadevanb, *J. Alloys Compd.*, 763 (2018) 935-950.
 29. S. Bello-Teodoro, R. Pérez-Garibay and J. Bouchard, *Ind. Eng. Chem. Res.*, 53 (2014) 7965-7970.
 30. Y. Li, H. Fu, Y. Zhang, Z. Wang and X. Li, *J. Phys. Chem. C*, 118 (2014) 6604-6611.
 31. J. He, M. Wang, W. Wang, R. Miao, W. Zhong, S.Y. Chen, S. Poges, T. Jafari, W. Song, J. Liu and S.L. Suib, *ACS Appl. Mater. Inter.*, 9 (2017) 42676-42687.
 32. S. Cao, N. Han, J. Han, Y. Hu, L. Fan, C. Zhou and R. Guo, *ACS Appl. Mater. Inter.*, 8 (2016) 6040-50.
 33. E. Yeager, *J. Mol. Catal.*, 38 (1986) 5-25.

34. A.S. Arico, Z. Poltarzewski, H. Kim, *J. Power Sources*, 55 (1995) 159-165.
35. Z. Zhang, D. Zhou, X. Bao, G. Huang, Q. Tang, B. Huang, *J. Alloys Compd.*, 777 (2019) 872-876.
36. A. Parthasarathy, S. Srinivasan, A.J. Appleby, C.R. Martin, *J. Electroanal. Chem.*, 339 (1992) 101-876.
37. S. Srinivasan, O.A. Velev, A. Parthasarathy, D.J. Manko, A.J. Appleby, *J. Power Sources*, 36 (1991) 299-320.
38. B.B. Zhang, H. Chen, Q. Daniel, B. Philippe, *ACS Catal.*, 7 (2017) 6311-6322.

© 2019 The Authors. Published by ESG (www.electrochemsci.org). This article is an open access article distributed under the terms and conditions of the Creative Commons Attribution license (<http://creativecommons.org/licenses/by/4.0/>).